Supporting Information

Potassium fluoride-induced FeOOH formation in NiFe oxalate for improved oxygen evolution performance

Seungjoon Ha,[a] Youngji Kim,[a] Taeyeop Kim,[a] Seongwoo Jeong,[a] Gyeong Hee Ryu,[b] and Seunghwa Lee*,[a]

[a] Department of Chemical Engineering, Changwon National University, 51140 Changwon, Republic of Korea.

[b] Department of Materials Engineering and Convergence Technology, Gyeongsang National University, Jinju 52828, Republic of Korea

*corresponding author

e-mail: seunghwa@changwon.ac.kr

Experimental

Materials synthesis

A Ni foil (99.5%, 0.1 mm thick, Thermo Fisher Scientific) was cleaned by immersion and sonication in 0.1 M HCl (DUKSAN reagent) for 30 minutes to eliminate the naturally formed Ni oxide layer and other contaminants. Subsequently, NiFe oxalates were synthesized directly on the cleaned Ni foil surface by immersing it in ethanolic oxalic acid solutions. The solution, composed of 1.0 M oxalic acid (DAEJUNG) and 0.01 M $FeCl_3$ (Thermo Scientific), was prepared in a 45% deionized water (DAEJUNG) and 55% ethanol (DUKSAN reagent) mixture, with varying concentrations of potassium fluoride (KF, 99%, Thermoscientific) ranging from 5 mM to 300 mM. The synthesis process proceeded for 1 hour at room temperature with stirring.

Electrochemical tests

Electrochemical tests were conducted using a potentiostat (VSP, Bio-Logic SAS) in a standard three-electrode cell at room temperature. The synthesized oxalates served as the working electrode, and a platinum wire was used as the counter electrode. A mercury-mercuric oxide (Hg/HgO) electrode served as the reference electrode. All measured potentials were converted to the reversible hydrogen electrode (RHE) using the formula: E (V vs RHE) = E (V vs Hg/HgO) + 0.098 + 0.059 × pH. Linear sweep voltammetry (LSV) was employed to assess the samples' activities at a scan rate of 1 mV sec^{-1} and obtain Tafel slopes. Cyclic voltammetry (CV) was performed with a scan rate of 40 mV sec^{-1} in the potential range of 1.2 V to 1.65 V. Before measurements, the current interrupt (CI) method available in the potentiostat software was utilized for Ohmic drop correction at a rate of 95%. Electrochemical impedance spectroscopy (EIS) measurements were performed with an amplitude of 10 mV in a frequency range from 100 kHz to 100 mHz. The EIS data of each sample was measured at a constant potential of 1.5 2V in 1 M KOH.

Characterization

The crystal structure analysis of the sample was conducted using X-ray diffraction (XRD, SmartLab SE instrument, Rigaku). Samples were positioned on a zero diffraction plate and analyzed with a 2.2 kW Kα (λ=1.54056 Å) X-ray source. X-ray photoelectron spectroscopy (XPS, AXIS SUPRA+, Kratos Analytical Ltd.), was employed to investigate the chemical state and elemental composition of the sample surface. Electrode samples were probed using a monochromated Al Kα excitation source (1,486 eV), with the adventitious carbon 1s peak serving as a calibration reference and internal standard. XPS data were obtained and analyzed using the Versatile ESCApe software. Surface morphology analysis was carried out via scanning electron microscopy (SEM, JSM-7900F, JEOL Ltd.). The corresponding elemental distribution was obtained through energy-dispersive X-ray spectroscopy (EDS) mapping. Transmission electron microscopy (TEM) analysis was conducted using TF30ST (Thermo Fisher) operated at 300 kV and EDS mapping was conducted using AZtecTEM with Ultim TEM.

Operando Raman experiments were conducted using a custom-made electrochemical Teflon cell at room temperature. The Raman microscope (XperRAM S, Nanobase) was connected to a 60X water-immersed objective (Olympus), and the excitation light source had a wavenumber

of 633 nm with a grating of 600 mm^{-1}. Each spectrum was acquired with a resolution of 1 cm^{-1}, comprising 20 consecutive scans with a 0.8 s exposure time per scan. For high confidence and reproducibility in the obtained spectra, peak shifts were calibrated using the peaks of the acetaminophen standard prior to the experiment. The counter electrode was a platinum wire, and the reference electrode was a double-junction Ag/AgCl electrode in a 3 M KCl solution. Raman signals were recorded in situ at open circuit potential (OCP) and under various applied potentials ranging from 1.2 V to 1.45 V versus RHE with a 0.05 potential step.

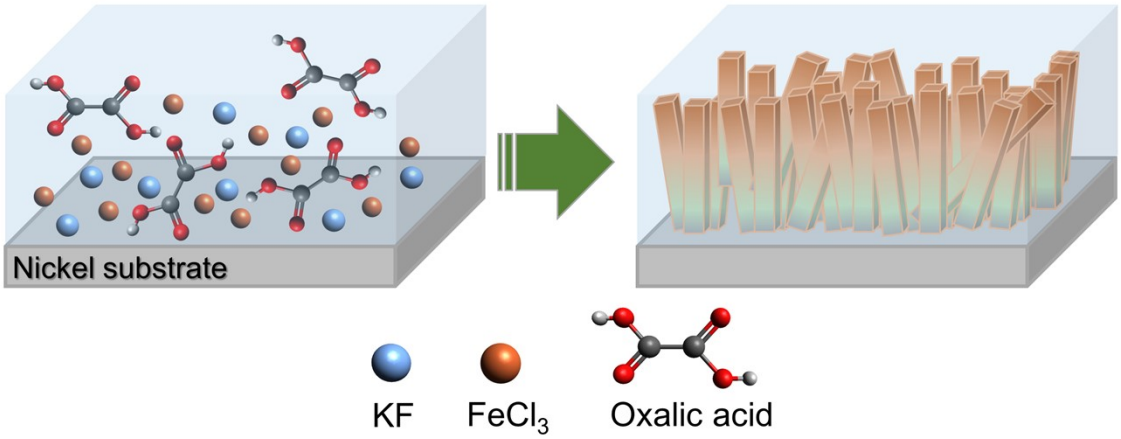

Figure S1. Scheme of in-situ synthesis of NiFe oxalate nanorods using a solution containing KF, $FeCl_3$, and oxalic acid on the surface of Ni foil.

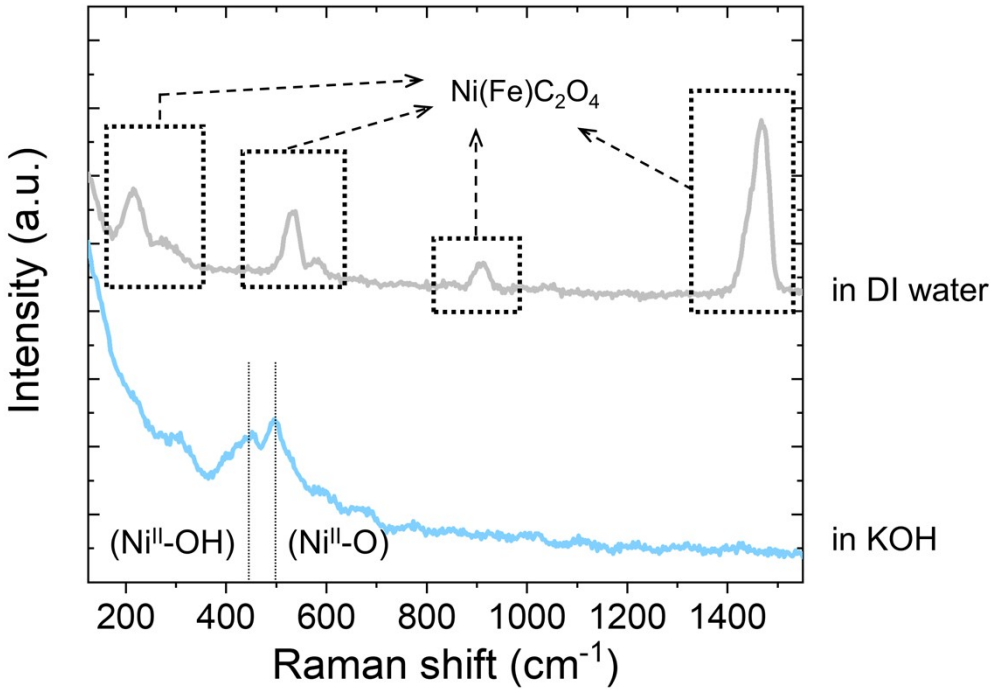

Figure S2. Raman spectra of OD-NiFe obtained before and after immersion in KOH.

Table S1. Summary of previous studies on OER catalysts derived from oxalate as a pre-catalyst.

Catalysts	Substrate	Overpotential (mV)	Current density (mA cm^{-2})	Tafel slope ($mV\ dec^{-1}$)	Ref.
F_{10}-OD-NiFe	Ni foil	226	10	~40	This work
$NiFe(OH)_{x-10}$	Ni foam	260	50	54	[1][1]
$NiFeC_2O_4$	Ni foam	210	50	53	[2][2]
$(Ni_{0.7}Fe_{0.3})C_2O_4$	Ni foam	203	50	43	[3][3]
$(Fe_{0.5}Ni_{0.5})C_2O_4$	Ni foam	284	50	54	[4][4]
NiFe-C_2O_4 LDH	Ni foam	265	500	41.58	[5][5]
$Fe(ox)(H_2O)_2$-(-1.4)-15	Ni foam	270	40	135	[6][6]
$Ni_{2.5}Co_5C_2O_4$	Carbon paper	330	10	81	[7][7]
Vs-$FeS_2/Cu_{39}S_{28}$	Cu foam	270	10	56.4	[8][8]
FNS-2OX	Ni foam	260	100	57	[9][9]

Table S2. Summary of previous studies on OER catalysts enhanced by fluorine doping.

catalysts	substrate	Overpotential (mV)	Current density (mA cm^{-2})	Tafel slope (mV dec^{-1})	Ref.
F_{10}-OD-NiFe	Ni foil	226	10	~40	This work
Fe-F-NiO_xH_y	Ni foil	322	10		[10][10]
F-NiFe-A	Ni foam	218	10	31	[11][11]
Re-NiFe-F	Ni foam	152	10	93.6	[12][12]
Mn-F/$Ni(OH)_2$	Ni foam	233	20	56.9	[13][13]
FeNiF	NCF (N-doped porous nanofibers)	260	10	67	[14][14]
Fe-CoF2-300	GC	230	10	41.9	[15][15]
CoFe@NCNTs-700-F-300	N-doped CNT	231	10	45.9	[16][16]
Ni-7.2 at. % Fe	Ni plate	260	10	53	[17][17]
NF-NCFO	GC	250	70	56	[18][18]

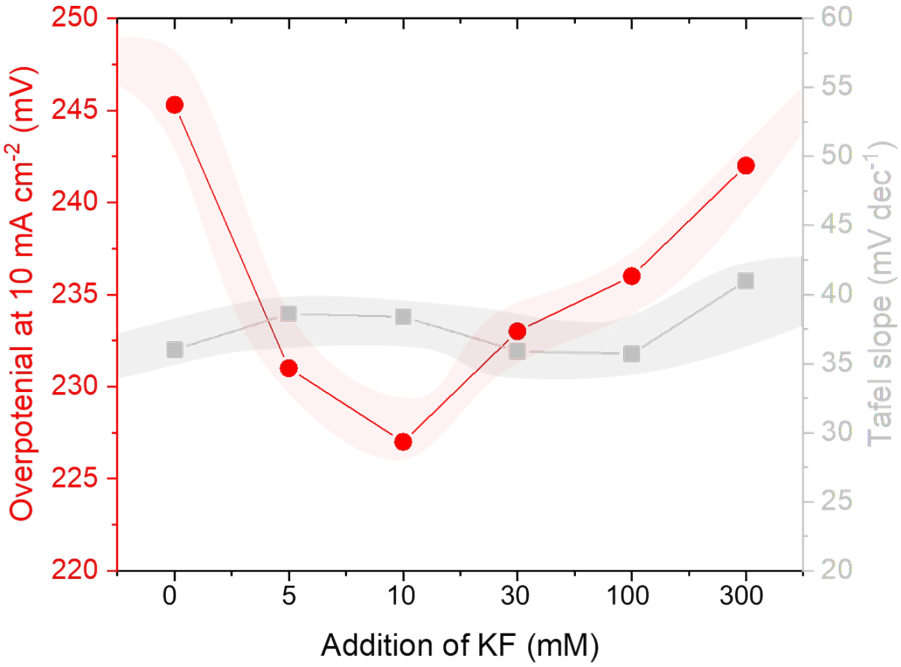

Figure S3. Comparison of overpotential at a current density of 10 mA cm^{-2} and Tafel slope.

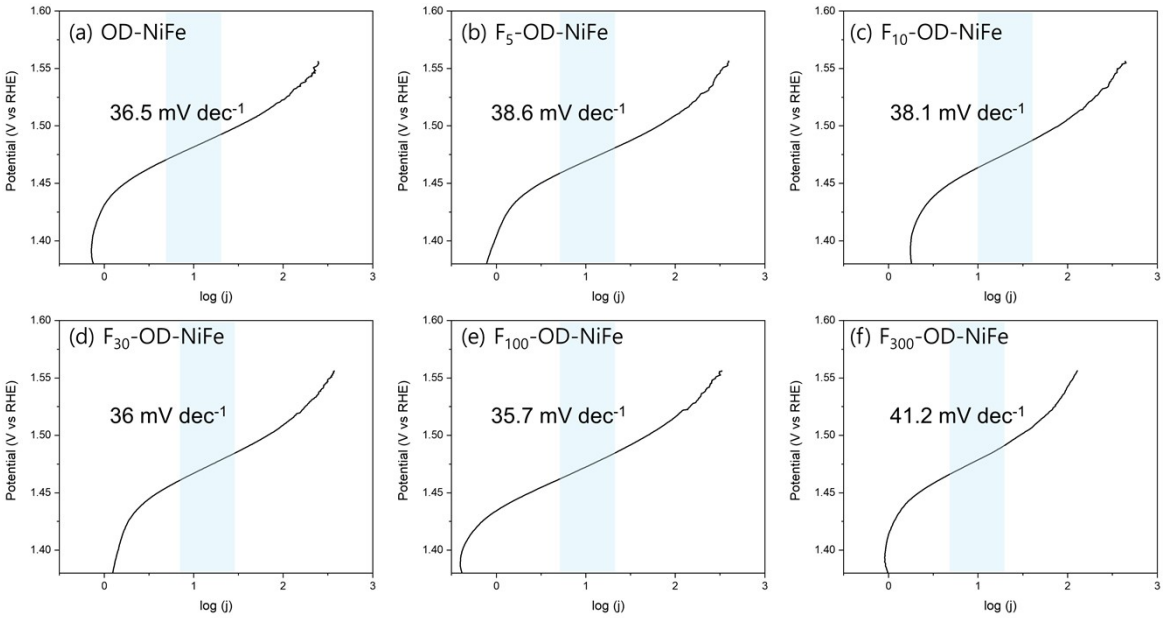

Figure S4. Tafel plots for OD-NiFe samples synthesized in solutions with KF concentrations ranging from 0 mM to 300 mM.

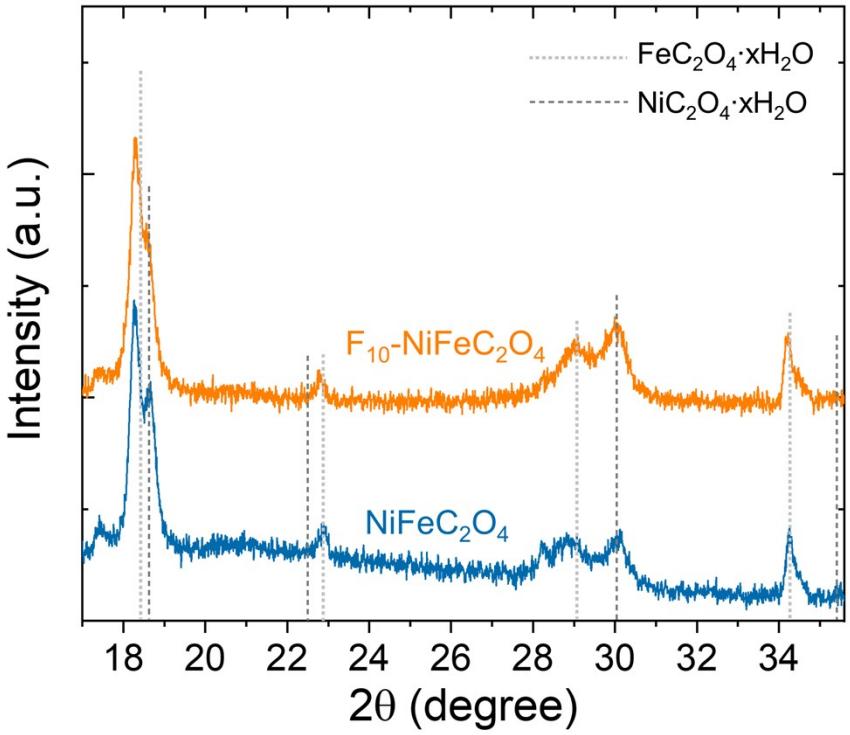

Figure S5. XRD patterns of oxalate samples synthesized from solutions with 0 and 10 mM of KF. The peaks corresponding to $NiC_2O_4 \cdot xH_2O$ and $FeC_2O_4 \cdot xH_2O$ were identified using JCPDS no. 25-0581 and no. 22-0635, respectively.

The peak at 18.4° for both $NiFeC_2O_4$ samples appeared at a lower 2-theta degree compared to the reference peak of $FeC_2O_4 \cdot xH_2O$, indicating a lattice expansion due to the incorporation of Ni as a dopant. This shift suggests that the structure of the synthesized bimetallic oxalates, whether with or without the addition of KF, has a slightly larger lattice compared to commercial FeC_2O_4 nanorods. Additionally, other minor peaks did not align perfectly with the reference oxalate peaks, further indicating modifications in the crystal structure.

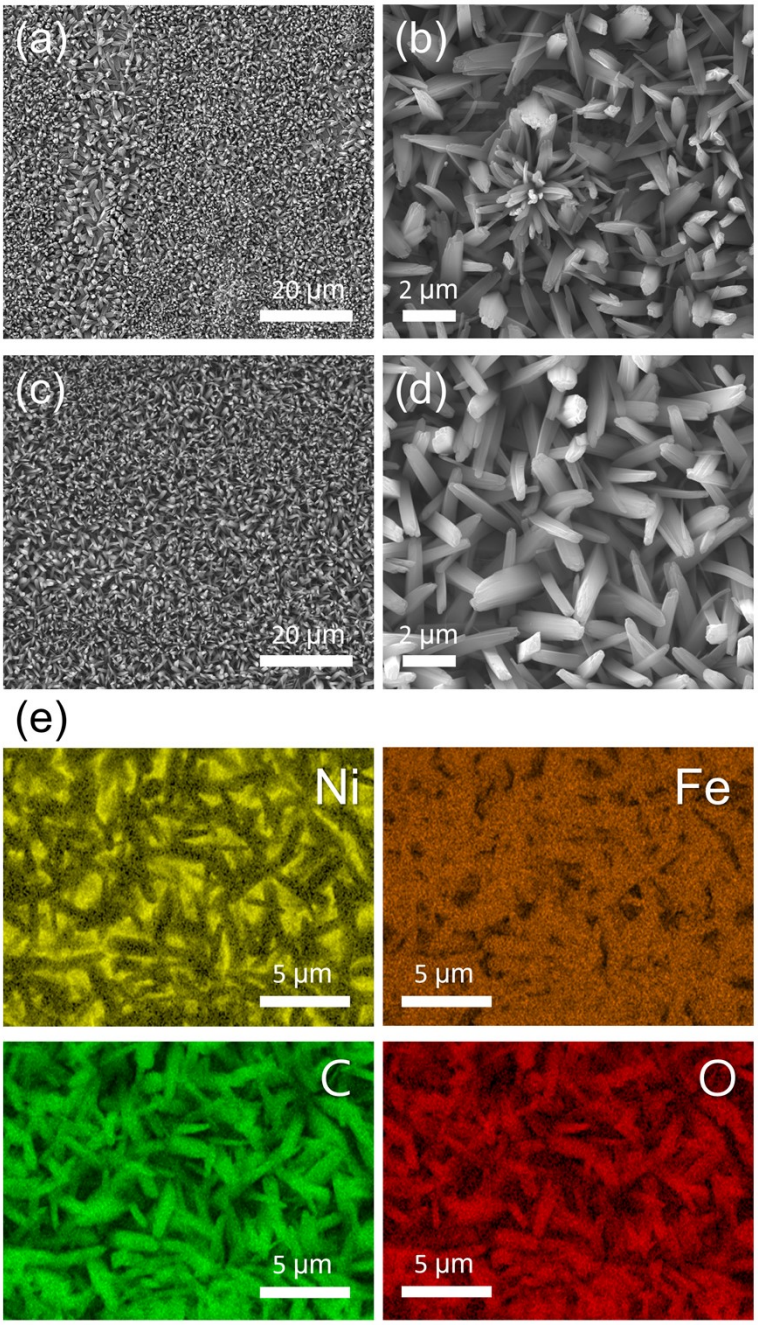

Figure S6. SEM images depicting both low magnification (a, c) and high magnification (b, d) views of (a, b) OD-NiFe and (c, d) F10-OD-NiFe. (e) EDS mapping analysis of F10-OD-NiFe, illustrating elemental distribution, including Ni, Fe, C, and O.

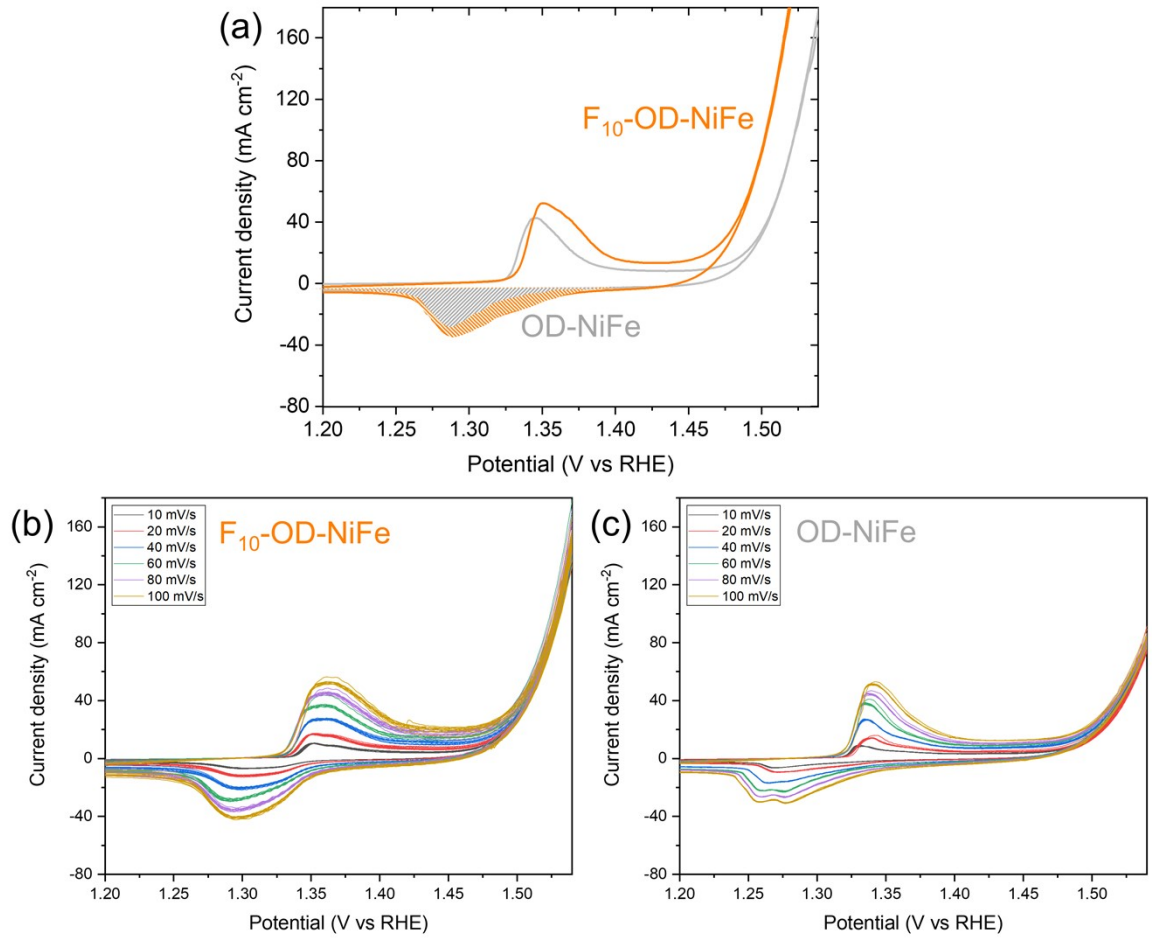

Figure S7. (a) CV curves of F_{10}-OD-NiFe (orange) and OD-NiFe (gray) obtained at a scan rate of 40 mV sec^{-1} in 1 M KOH. (b) CV curves of F_{10}-OD-NiFe and (c) OD-NiFe obtained at different scan rates from 10 to 100 mV sec^{-1}.

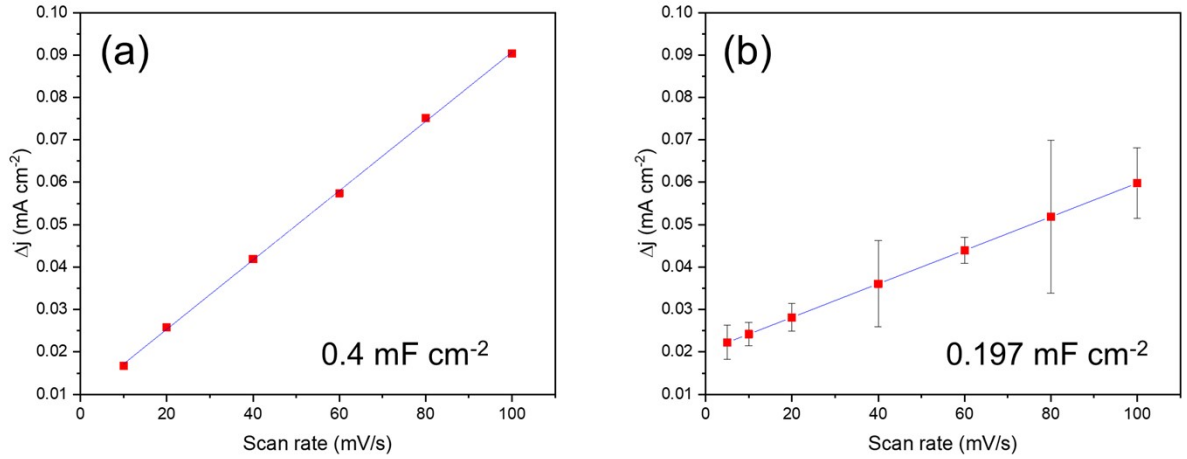

Figure S8. Plots depicting the difference of anodic and cathodic current densities, ΔJ=|ja-jc|, against the scan rate (10, 20, 40, 60, 80, 100 mV sec^{-1}) for (a) F_{10}-OD-NiFe and (b) OD-NiFe samples. The estimated double-layer capacitances (C_{dl}) for the were calculated as 0.4 and 0.197 mF cm^{-2} respectively.

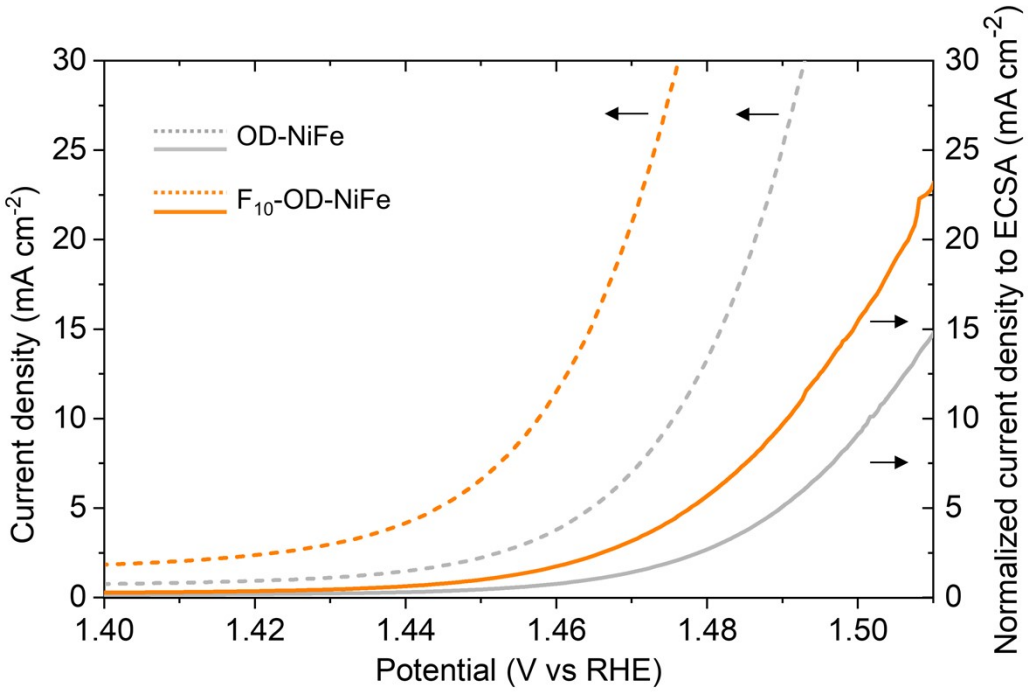

Figure S9. LSV curves before and after normalization to electrochemical surface area (ECSA) for OD-NiFe (gray) and F_{10}-OD-NiFe (orange).

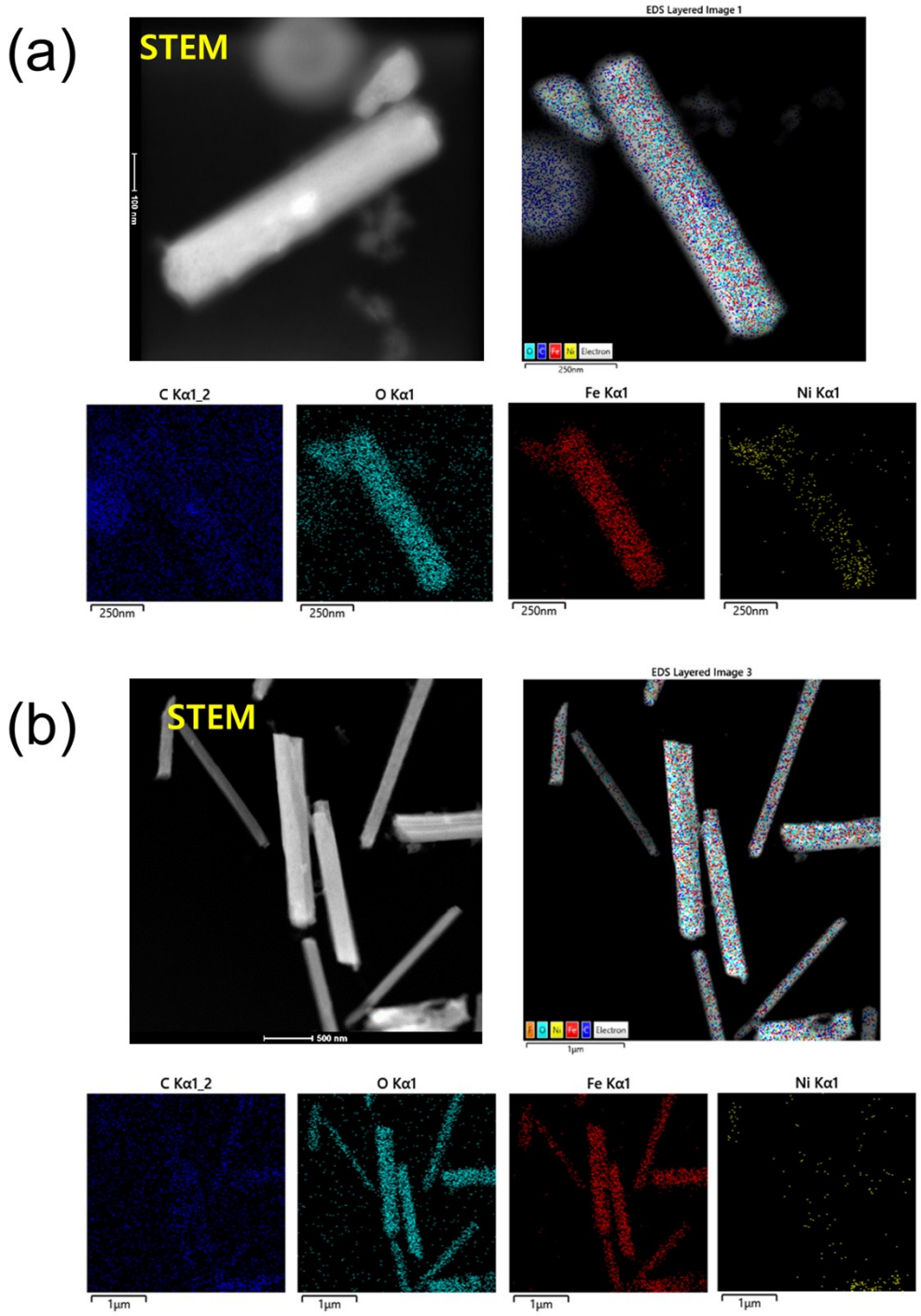

Figure S10. TEM images and the corresponding EDS mapping results of (a) OD-NiFe and (b) F_{10}-OD-NiFe samples.

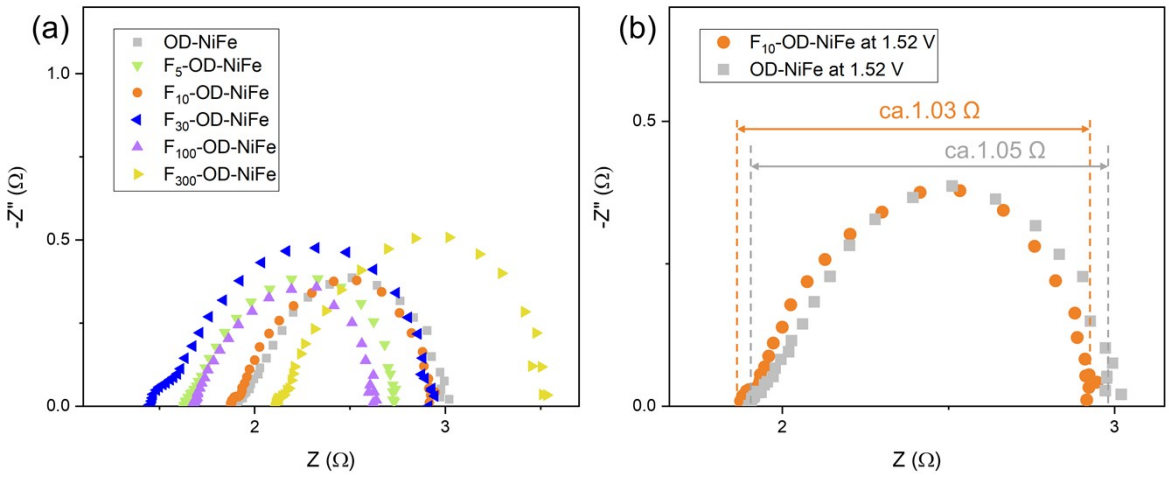

Figure S11. Nyquist plots obtained during OER at 1.52 V showing (a) synthesized OD-NiFe samples and (b) a comparison of charge transfer resistance between OD-NiFe and F_{10}-OD-NiFe.

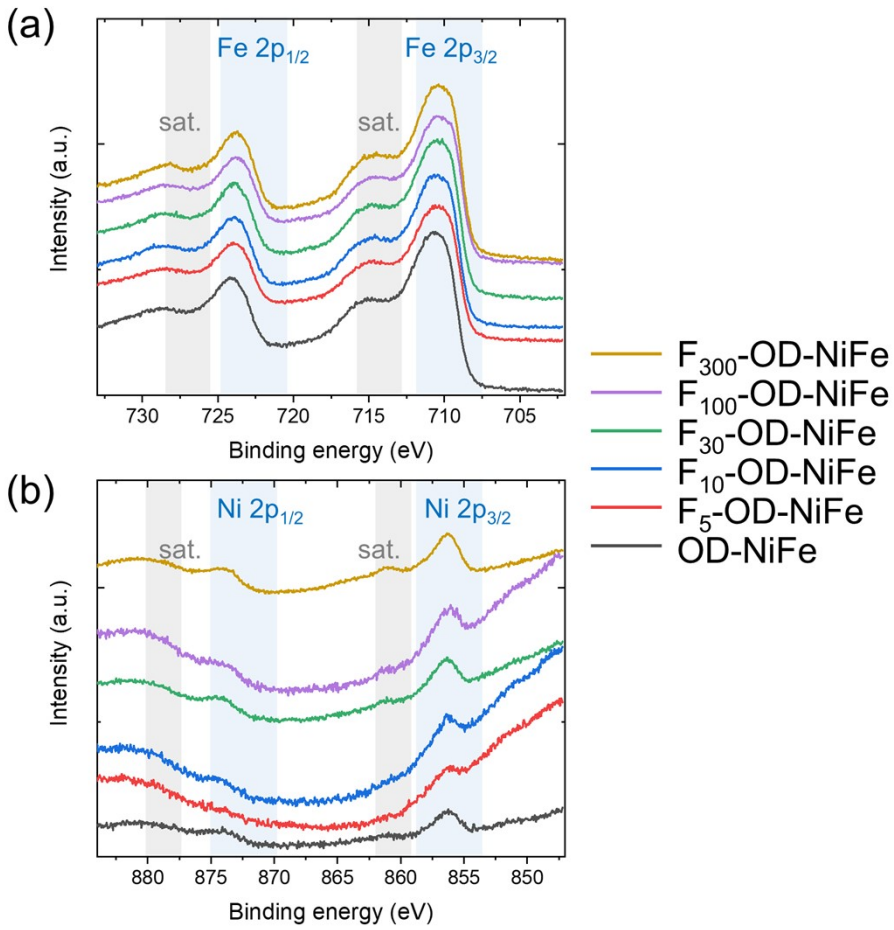

Figure S12. XPS spectra of the synthesized samples showing (a) Fe 2p and (b) Ni 2p regions.

Although XPS surface analysis was conducted, as shown in Figure S12, discerning differences in the Fe 2p spectra, whether KF is used or not, proved challenging. This difficulty arises from the similarities in binding energies and spectral shapes among higher oxides of iron, making it impossible to definitively assign the iron species as higher oxides or oxyhydroxides such as Fe_2O_3 and FeOOH using XPS alone. Therefore, we supplemented our study with operando Raman spectroscopy analysis to further investigate these species.[19]

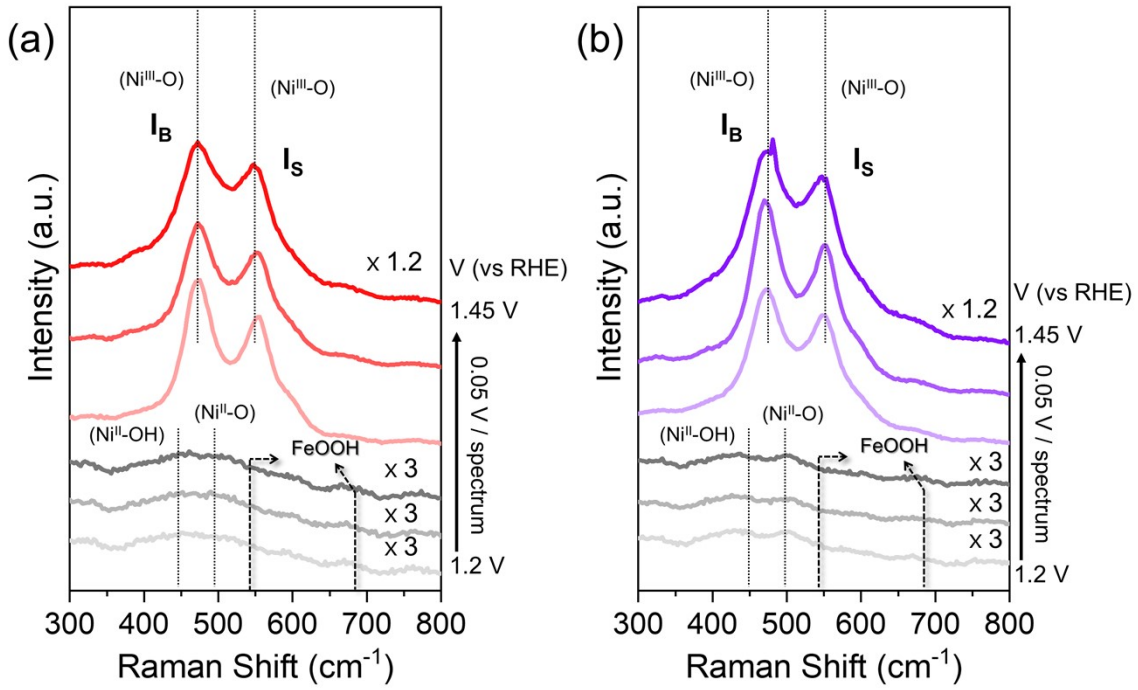

Figure S13. Operando Raman spectra of (a) F_{30}-OD-NiFe and (b) F_{100}-OD-NiFe acquired as a function of applied potential ranging from 1.2 V to 1.45 V with a 0.05 potential step.

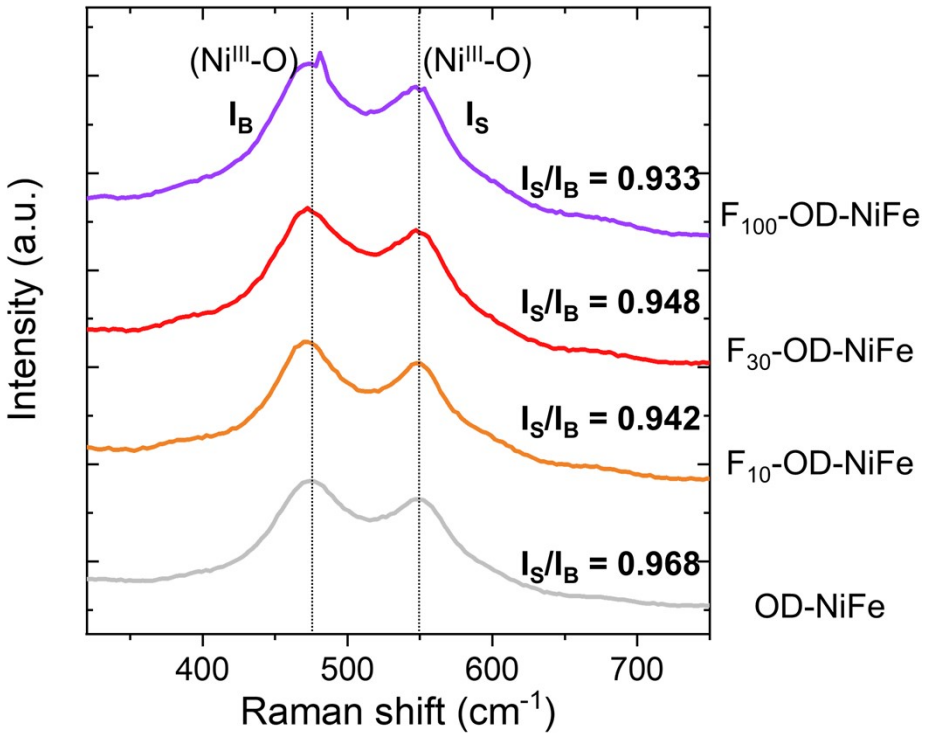

Figure S14. Operando Raman spectra illustrating the different I_S/I_B values of the OD-NiFe samples at 1.45 V.

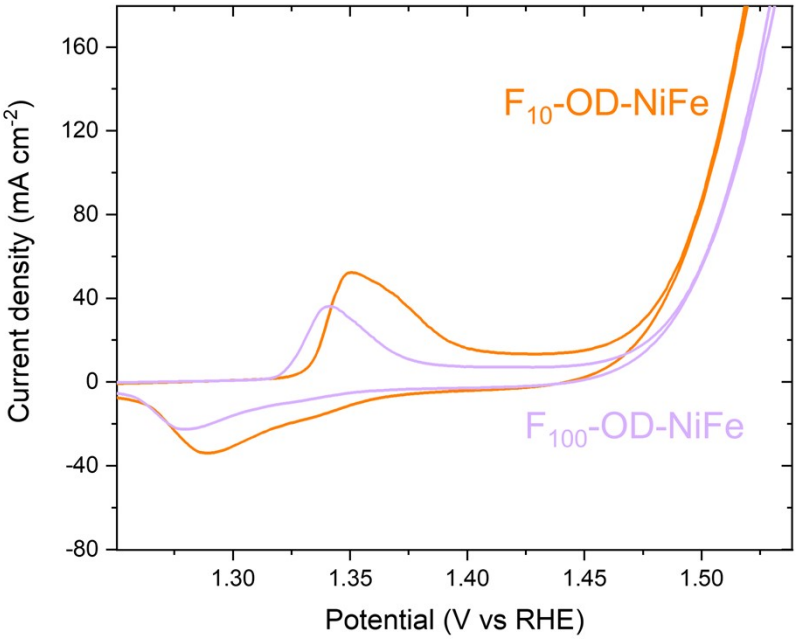

Figure S15. CV curves of F_{10}-OD-NiFe (orange) and F_{100}-OD-NiFe (light violet) obtained at a scan rate of 40 mV sec^{-1} in 1 M KOH.

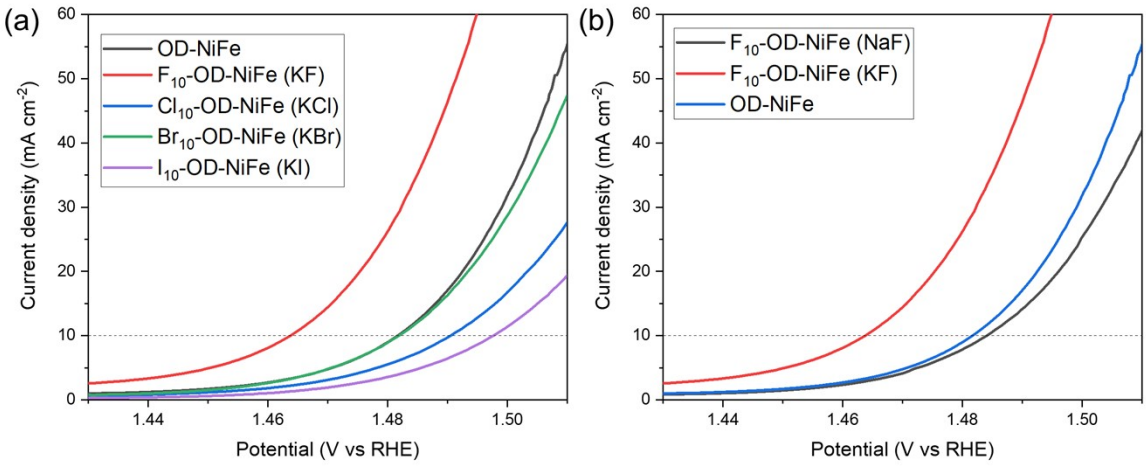

Figure S16. LSV curves of OD-NiFe samples synthesized in solutions containing KF, KCl, KBr, and KI. (b) LSV curves of another F_{10}-OD-NiFe synthesized in a NaF-containing oxalic acid instead of KF. All the curves were obtained at a scan rate of 40 mV sec^{-1} in 1 M KOH.

Appendix 1

During the oxidation of $Ni(OH)_2$ to NiOOH, Raman spectroscopy analysis typically reveals a pair of bands around 480 and 560 cm^{-1}. The 560 cm^{-1} peak is attributed to the polarized A_{1g} mode (stretching), while the 480 cm^{-1} peak corresponds to the depolarized E_g mode (bending) of NiOOH.[20,21] In the A_{1g} mode, the oxygen atoms vibrate perpendicular to the plane of oxygen, whereas in the E_g mode, they vibrate along this plane. The intensities and positions of these peaks provide insights into changes in the local Ni-O structure, such as lattice disorder within the sheets and the interlayer spacing between them.[22]

This I_B/I_S ratio has been linked to the structural disorder of NiOOH, where a higher ratio indicates greater structural disorder. For example, as more Fe is incorporated into the NiOOH lattice, it causes distortions in the sheets that form the layered structure of NiOOH.[22,23] This leads to increased overall structural disorder, which is reflected in the intensity ratio of the two Raman peaks. Therefore, if an increase in the I_B/I_S ratio is observed while assuming a consistent amount of Fe doping, it suggests that more Fe has penetrated into the bulk region rather than remaining at the surface. Generally, according to previous studies, when the Fe content in NiFe oxides ranges from about 5% to 50%, this I_B/I_S ratio typically varies from approximately 0.7 to 1.[22,23]

In conclusion, the Fe content approaches 80% for the sample we synthesized, yet the I_B/I_S ratio converges to about 0.95. This suggests that Fe is predominantly distributed on the surface rather than in the bulk of the material.

References

1 J. Ha, M. Kim, Y.-T. Kim and J. Choi, *ACS Appl. Mater. Interfaces*, 2021, **13**, 42870–42879.

2 P. Babar, K. Patil, V. Karade, K. Gour, A. Lokhande, S. Pawar and J. H. Kim, *ACS Appl. Mater. Interfaces*, 2021, **13**, 52620–52628.

3 X. Gao, D. Chen, J. Qi, F. Li, Y. Song, W. Zhang and R. Cao, *Small*, 2019, **15**, 1904579.

4 H. Hu, X. Lei, S. Li, R. Peng and J. Wang, *New Journal of Chemistry*, 2022, **46**, 328–333.

5 P. Hao, W. Zhu, F. Lei, X. Ma, J. Xie, H. Tan, L. Li, H. Liu and B. Tang, *Nanoscale*, 2018, **10**, 20384–20392.

6 Y. Hai, L. Liu and Y. Gong, *Inorg. Chem.*, 2021, **60**, 5140–5152.

7 S. Ghosh, R. Jana, S. Ganguli, H. R. Inta, G. Tudu, H. V. S. R. M. Koppisetti, A. Datta and V. Mahalingam, *Nanoscale Adv.*, 2021, **3**, 3770–3779.

8 F. Wei, J. Shen, J. Gong, Q. Peng, L. Shi, T. T. Isimjan and X. Yang, *J. Phys. Chem. Lett.*, 2024, **15**, 1172–1180.

9 W. Xu, C. Zhang, H. Shen, X. Ma, Z. Cheng, J. Wu, Q. Zhu, J. Lin, Z. Fu and H. Deng, *ACS Sustain. Chem. Eng.*, 2022, **10**, 14396–14406.

10 Y. Jang, S. Ha, H.-T. Lim and S. Lee, *Chem. Commun.*, 2023, **59**, 8298–8301.

11 Q. Xu, H. Jiang, X. Duan, Z. Jiang, Y. Hu, S. W. Boettcher, W. Zhang, S. Guo and C. Li, *Nano Lett.*, 2021, **21**, 492–499.

12 S. Cai, H. Liu, H. Cheng, B. Sun, W. Xia, H. Hu and S. Zhou, *ACS Appl. Nano Mater.*, 2023, **6**, 7864–7872.

13 J. Lv, X. Yang, K. Li, X. Chen, S. Sun, H.-Y. Zang, Y.-F. Chang, Y.-H. Wang and Y.-G. Li, *Nanoscale Adv.*, 2019, **1**, 4099–4108.

14 M. Zha, C. Pei, Q. Wang, G. Hu and L. Feng, *J. Energy Chem.*, 2020, **47**, 166–171.

15 M. Li, Y. Gu, Y. Chang, X. Gu, J. Tian, X. Wu and L. Feng, *Chem. Eng. J.*, 2021, **425**, 130686.

16 Y. Kuang, R. He, X. Gu, F. Yang, X. Tian and L. Feng, *Chem. Eng. J.*, 2023, **456**, 141055.

17 N. Yamada, S. Kitano, Y. Yato, D. Kowalski, Y. Aoki and H. Habazaki, *ACS Appl. Energy Mater.*, 2020, **3**, 12316–12326.

18 H. Han, J. Woo, Y.-R. Hong, Y.-C. Chung and S. Mhin, *ACS Appl. Energy Mater*, 2019, **2**, 3999–4007.

19 F. Song, M. M. Busch, B. Lassalle-Kaiser, C. S. Hsu, E. Petkucheva, M. Bensimon, H. M. Chen, C. Corminboeuf and X. Hu, *ACS Cent. Sci.*, 2019, **5**, 558–568.

20 B. J. Trzes??niewski, O. Diaz-Morales, D. A. Vermaas, A. Longo, W. Bras, M. T. M. Koper and W. A. Smith, *J. Am. Chem. Soc.*, 2015, **137**, 15112–15121.

21 S. Lee, Y.-C. Chu, L. Bai, H. M. Chen and X. Hu, *Chem Catal.*, 2022, 100475.

22 S. Lee, L. Bai and X. Hu, *Angew. Chem. Int. Ed.*, 2020, **59**, 8072–8077.

23 M. W. Louie and A. T. Bell, *J. Am. Chem. Soc.*, 2013, **135**, 12329–12337.